

# Silicon orientations to grow semi-polar AlN

Received: 4 August 2024

Ji-Li Li <sup>1,3</sup>, Ye-Fei Li <sup>1,3</sup> ✉ & Zhi-Pan Liu <sup>1,2</sup> ✉

Accepted: 28 April 2025

Published online: 08 May 2025

Check for updates

The growth of non-polar GaN on Si substrates is a grand challenge in developing light-emitting diodes, where AlN layers serve as buffers to mitigate the lattice mismatch between GaN and Si in practice. Even though, the primary difficulty arises from the predominant growth of polar AlN(0001) layers. Here we demonstrate that stepped Si(320) can establish a high-quality interface with the semi-polar AlN(2241) as identified through machine-learning-based structure predictions that explored millions of potential interface configurations. This interface exhibits atomic-matching with low interface energy, and importantly, features reduced polarization (0.20 C/m<sup>2</sup>) along with superior interfacial thermal conductance (0.47 GWm<sup>-2</sup>K<sup>-1</sup>).

The epitaxial growth of crystals over the Si substrate represents a crucial method for producing functional materials as semiconducting devices. This is particularly relevant in the context of growing wurtzite GaN on silicon substrates for high-brightness light-emitting diodes (LEDs)<sup>1–4</sup>, a market projected to reach USD 27.5 billion by 2023 and anticipated to grow at a Compound Annual Growth Rate (CAGR) exceeding 9% from 2024 to 2032<sup>5</sup>. Due to the significant lattice mismatch between GaN and Si (-16% strain), an AlN buffer layer with a wurtzite structure is essential for guiding the orientation of subsequent GaN layers (see Fig. 1a). However, AlN predominantly grows along the polar AlN[0001] direction<sup>6–10</sup>, resulting in substantial polarization perpendicular to the AlN/GaN layers, which constrains the quantum efficiency of LEDs<sup>11–14</sup>. In recent years, significant efforts have been made by both academia and industry to find solutions to reduce the polarization; however, no successful methods has been reported in directly growing non-polar or semi-polar AlN, not even mentioning to maintain simultaneously other desired interface properties such as high stability and excellent thermal conductance necessary for long lifespan. Modulating the orientation of epitaxial crystals remains a fundamental challenge<sup>15–17</sup>, largely relying on trial-and-error experimental tests.

Experiments have shown that AlN growth on all low Miller index Si substrates, including Si(111), (110), and (100), exclusively adheres to the polar AlN(0001) orientation<sup>6–8,10,18–21</sup>. To obtain better quality AlN, a Al-rich growth protocol was commonly adopted<sup>22</sup>, where Si is first exposed to Al(CH<sub>3</sub>)<sub>3</sub> for Al deposition followed by the controlled nitridation using NH<sub>3</sub> to convert Al into AlN. Despite the process optimization, significant atomic mismatches remain at the Si/AlN interfaces. For

instance, the (111)<sub>Si</sub> || (0001)<sub>AlN</sub> interface has a large mismatch with a 4:5 matching along Si[112] direction<sup>23</sup>. A similar magnitude of misfit dislocation occurs at the (110)<sub>Si</sub> || (0001)<sub>AlN</sub> interface along Si[110] direction<sup>24</sup>. This raises an intriguing question regarding whether there are perfectly matched Si/AlN interfaces that should ideally be non-polar and semipolar.

A key characteristic of non-polar AlN crystalline layers is that their Miller index {hki} must possess normal vectors perpendicular to the polar direction [0001]. In this context, higher index Si(n11) surfaces<sup>25,26</sup> show potential for growing semi-polar or non-polar AlN. However, the experimental tests on (311)<sub>Si</sub> || (1122)<sub>AlN</sub><sup>27</sup> still reveal considerable defects and dislocations<sup>12,14,28,29</sup>, rendering them unsuitable for applications. Given the vast array of high-index Si orientations and diverse growth conditions, it has historically been challenging to investigate all possible solid-solid interface structures with varying chemical compositions due to the lack of efficient theoretical tools.

Herein, we present a theoretical prediction of a high-index Si orientation that enables the growth of AlN with low polarization and high interfacial thermal conductance (ITC). The prediction is achieved through an exhaustive interface structure screening using our recently developed machine-learning-based interface search (ML-interface) method<sup>30,31</sup>, which integrates lattice-matched orientation relationship (OR) screening with global optimization based on machine-learning potential.

## Results and discussion

In this work, we have explored 9530 likely interface compositions and finally identified 1625 lattice-matched Si/AlN interfaces with the strain less than 5.0%. Among them, 28 interfaces are confirmed to have an

<sup>1</sup>State Key Laboratory of Porous Materials for Separation and Conversion, Collaborative Innovation Center of Chemistry for Energy Material, Shanghai Key Laboratory of Molecular Catalysis and Innovative Materials, Key Laboratory of Computational Physical Science, Department of Chemistry, Fudan University, Shanghai 200433, China. <sup>2</sup>State Key Laboratory of Metal Organic Chemistry, Shanghai Institute of Organic Chemistry, Chinese Academy of Sciences, Shanghai 200032, China. <sup>3</sup>These authors contributed equally: Ji-Li Li, Ye-Fei Li. ✉ e-mail: [yefei@fudan.edu.cn](mailto:yefei@fudan.edu.cn); [zpliu@fudan.edu.cn](mailto:zpliu@fudan.edu.cn)

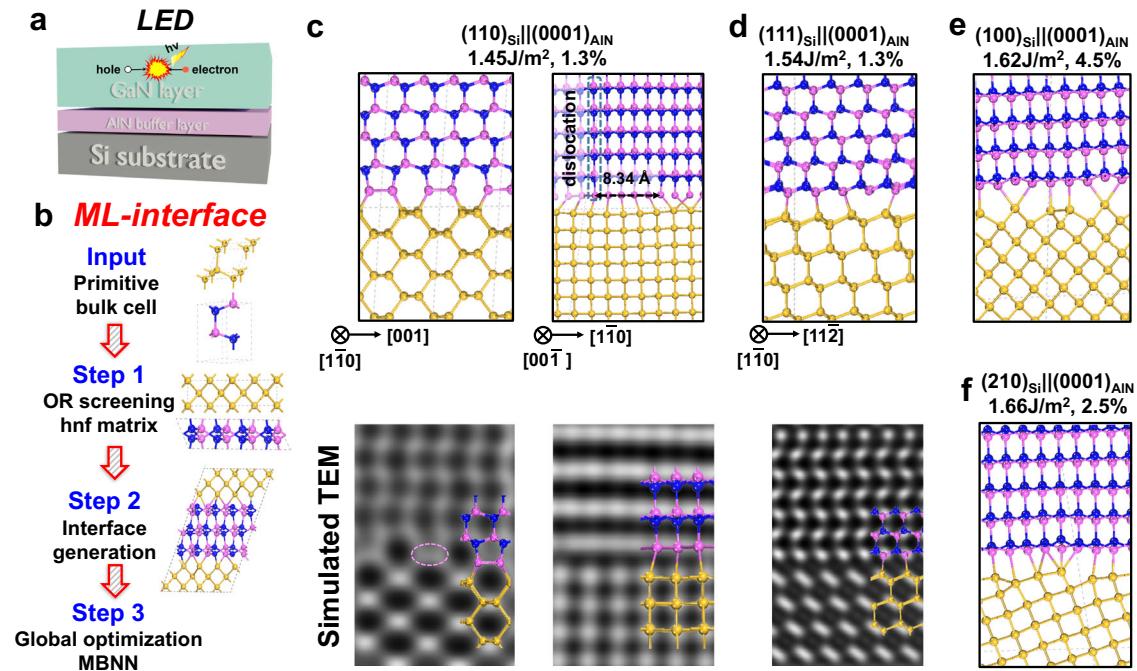


**Fig. 1 | ML-interface method and the determined polar Si/AlN interfaces.** **a** Structure of GaN/AlN/Si LEDs. **b** Schematic representation of the ML-interface method. **c–f** Atomic structures of four polar Si/AlN interfaces. Simulated transmission electron microscopy (TEM) images for  $(110)_{\text{Si}}||((0001)_{\text{AlN}})$  and  $(111)_{\text{Si}}||$

$(0001)_{\text{AlN}}$  are shown at the bottom of **(c)** and **(d)**. The widths of the simulated TEM images are 1.6, 1.0, and 1.8 nm. The purple dashed circles in TEM images represent the additional Al layer at the interface. Colors in the figure: Yellow balls are Si; violet balls are Al; blue balls are N.

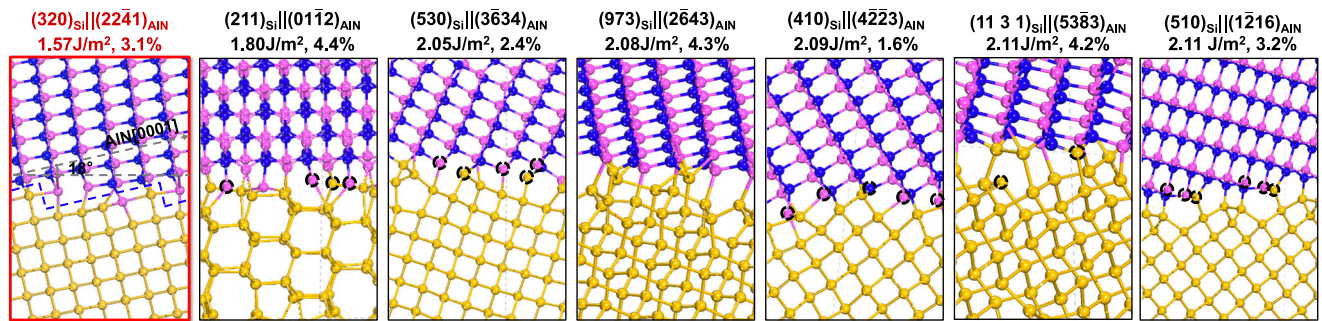


**Fig. 2 | Atomic structures of 7 low-polar Si/AlN interfaces ranked by the interface energies.** The black dashed circles highlight unsatisfied atoms with dangling bonds. In the  $(320)_{\text{Si}}||((2241)_{\text{AlN}})$  interface, blue dashed lines highlight the

stepped interface, while gray dashed lines denote the angle between the Al[0001] direction and the interface plane. Yellow balls are Si; violet balls are Al; blue balls are N.

interface energy ( $\gamma_{\text{int}}$ ) below  $2.2\text{J}/\text{m}^2$ , which are obtained by SSW global optimization for more than 1,570,000 minima. It should be mentioned that we have considered various chemical compositions for every interface, from which the most stable interface, the global minimum (GM), is obtained by using the bulk Al and Si as the reference to define the chemical potential of Al and Si, respectively (see Supplemental Note 2 for details).

These 28 low-energy interfaces can be grouped into 11 distinct Si orientations and their interface structures, interfacial energy, and strains are presented in Fig. 1c–f and Fig. 2, categorized by the polarization of AlN layer. The polarization  $P_v$  of AlN perpendicular to the AlN layer is also computed using Eqs. 1–2 by measuring the angle with respect to the polar [0001] direction, where  $\mathbf{T}$  is the lattice parameter matrix of the AlN unit cell;  $d_{hkl}$  is the spacing of  $(hkl)$  planes<sup>30</sup>; and  $|P|$  is the spontaneous polarization in bulk AlN calculated using Berry phase method<sup>32</sup>. To account for the lattice scaling effect, we have calculated

$|P|$  using the lattice parameters of AlN at the Si/AlN interface that results in  $|P|$  values ranging from 1.27 to  $1.33\text{C}/\text{m}^2$ , being in fact close to the value of AlN crystal without lattice scaling ( $1.30\text{C}/\text{m}^2$ ). This is consistent with the low strain ( $<4.4\%$ ) fact of our identified interface models. The final  $P_v$  of the grown AlN layers is plotted in Fig. 3a.

$$P_v = [\mathbf{n}_{(hkl)} \cdot \mathbf{n}_{(0001)}] \times |P| \quad (1)$$

$$\frac{\mathbf{n}_{(hkl)}}{d_{hkl}} = (\mathbf{T})^{-1} \cdot \begin{pmatrix} h \\ k \\ l \end{pmatrix} \quad (2)$$

The four interfaces in Fig. 1 are formed between polar AlN and low-index Si (hereafter denoted as polar interface), specifically  $(110)_{\text{Si}}||$

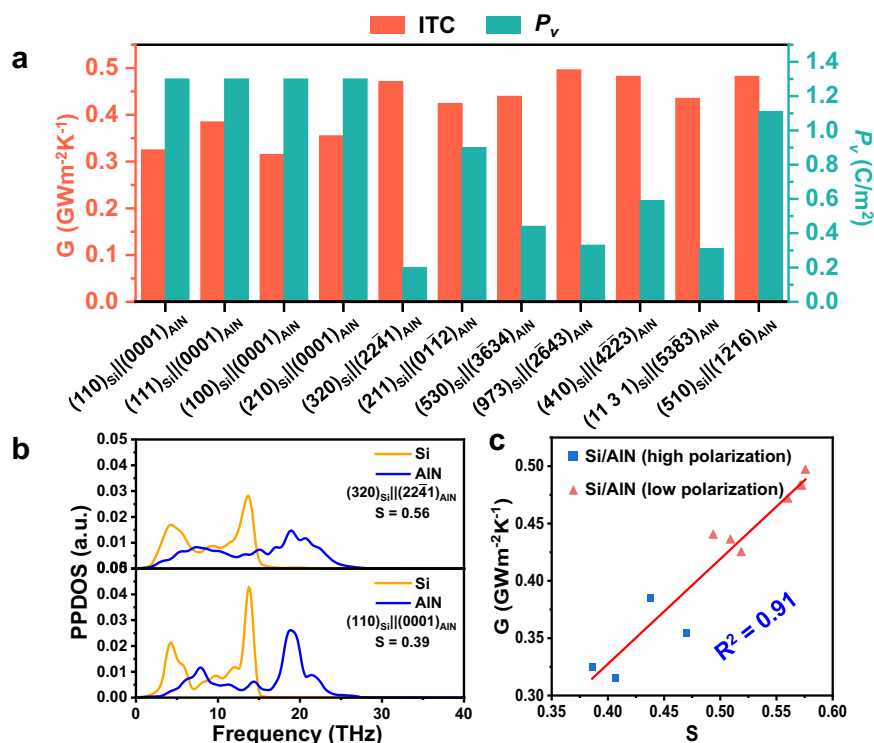


**Fig. 3 | Interfacial thermal conductance and polarization of Si/AlN interfaces.** **a** Interfacial thermal conductance (red bars) and polarization (cyan bars) for 11 Si/AlN interfaces. **b** Cross-interface-plane partial phonon density of states (PPDOS) in

arbitrary units (a.u.). **c** Correlation between interfacial thermal conductance (G) and phonon correlation factor (S).

(0001)<sub>AlN</sub>, (111)<sub>Si</sub>|(0001)<sub>AlN</sub>, (100)<sub>Si</sub>|(0001)<sub>AlN</sub>, and (210)<sub>Si</sub>|(0001)<sub>AlN</sub> with interfacial energies range from 1.45 to 1.66 J/m<sup>2</sup>. Following them are 7 interfaces (see Fig. 2) formed between semi-polar AlN and high-index Si surfaces (denoted as low-polar interface), with interfacial energies spanning from 1.57 to 2.11 J/m<sup>2</sup>. There is no interface available between non-polar AlN and Si. The low interface energy of polar interfaces is consistent with the experimental observations that the growth of AlN(0001) is more favorable than other AlN orientations<sup>7,16,24</sup>, indicating the preferential growth of AlN(0001) is a consequence of thermodynamic favorableness.

To demonstrate that our predicted interface atomic structures indeed include those observed in experiments, we compare the ORs and atomic arrangements of two polar interfaces, (110)<sub>Si</sub>|(0001)<sub>AlN</sub> and (111)<sub>Si</sub>|(0001)<sub>AlN</sub>, for which the TEM data of experiment are available<sup>16,33</sup>. As illustrated in Fig. 1c, d, our predicted interfaces exhibit abrupt atomic arrangements, resulting in a sharp interface as depicted in our TEM simulated image. It might be mentioned that the interfaces with Si-Al mixing layers (e.g. interfacial Si replacement by Al) have been verified, both from variable-composition SSW global search trajectories and from manually constructed configurations, which confirm that the mixed interfaces are less stable than the identified abrupt interface with additional Al layer (see Supplemental Note 3 for details).

Specifically, the ORs of the (110)<sub>Si</sub>|(0001)<sub>AlN</sub> interface indicate that the Si[110] and [001] directions align parallel to AlN[1120] and [1100] directions, respectively, which agrees with experimental TEM images. Importantly, the atomic configurations projected along Si[110] reveal an additional Al layer sandwiched between AlN and Si matrices. This interfacial metallic Al layer acts as an electron bath and compensates the boundary charge. This configuration leads to the characteristic Al-Al pair viewed from [110] forming above the trench of Si(110). This Al-Al pair appear as elongated a white spot from our simulated TEM (see purple dashed cycles in Fig. 1c), consistent with the large spot observed at the interface in the experimental results<sup>16,33</sup>. Conversely, both the atomic structures and simulated TEM projected

along Si[001] display a periodic dislocation with a separation of approximately 8 Å (refer to the blue dashed rectangle in Fig. 1c), mirroring findings from experimental observations<sup>33</sup>. Similarly, the ORs and atomic arrangements of the (111)<sub>Si</sub>|(0001)<sub>AlN</sub> interface match closely with those seen in the experimental TEM images<sup>16</sup>.

Now, we turn our attention to low-polar interfaces—an area of significant interest to the semiconductor industry. Notably, we identify 7 high-index Si faces—namely Si(320), (211), (530), (973), (410), (1131), and (510)—that can form lattice-matched interfaces with semi-polar AlN as shown in Fig. 2. The interface energies of these low-polar interfaces range from 1.57 to 2.11 J/m<sup>2</sup>, with polarization values spanning from 0.20 to 1.11 C/m<sup>2</sup> (refer to the cyan bars in Fig. 3a). The (320)<sub>Si</sub>|(2241)<sub>AlN</sub> interface demonstrates both the lowest interface energy (1.57 J/m<sup>2</sup>) and the lowest polarization (0.20 C/m<sup>2</sup>). Notably, the interface energy of (320)<sub>Si</sub>|(2241)<sub>AlN</sub> (1.57 J/m<sup>2</sup>) is comparable to that of (111)<sub>Si</sub>|(0001)<sub>AlN</sub> (1.54 J/m<sup>2</sup>), the most commonly used interface orientation in experiments. Furthermore, the Si(320) substrate exhibits stability characterized by a low surface energy of 1.39 J/m<sup>2</sup> which is comparable to that of Si(100) (1.40 J/m<sup>2</sup>) and has been successfully synthesized experimentally<sup>34</sup> (see Supplemental Note 5 for details). Collectively, these findings suggest that Si(320) serves as a promising substrate for growing Si/AlN/GaN LEDs. The reduced polarization of (320)<sub>Si</sub>|(2241)<sub>AlN</sub> interface can be attributed to the fact that the AlN[0001] direction in (2241)<sub>AlN</sub> forms a small angle (18.0°) with the interface plane, as shown in Fig. 2.

Interestingly, the (320)<sub>Si</sub>|(2241)<sub>AlN</sub> interface forms a unique ordered atomic structure, which could be verified in experiment. Both Si(320) and AlN(2241) are stepped surfaces. Specifically, the AlN(2241) surface comprises AlN(1120) terraces and minor AlN(0001) steps, while the Si(320) surface consists of Si(110) terraces and minor Si(110) steps. The step sites on Si(320) and AlN(2241) surfaces accidentally have almost identical heights (1.92 Å) and periodicities (1 nm), facilitating a smooth atomic matching at the interface. As shown in Fig. 2, all boundary atoms along the (320)<sub>Si</sub>|(2241)<sub>AlN</sub> interface maintain their

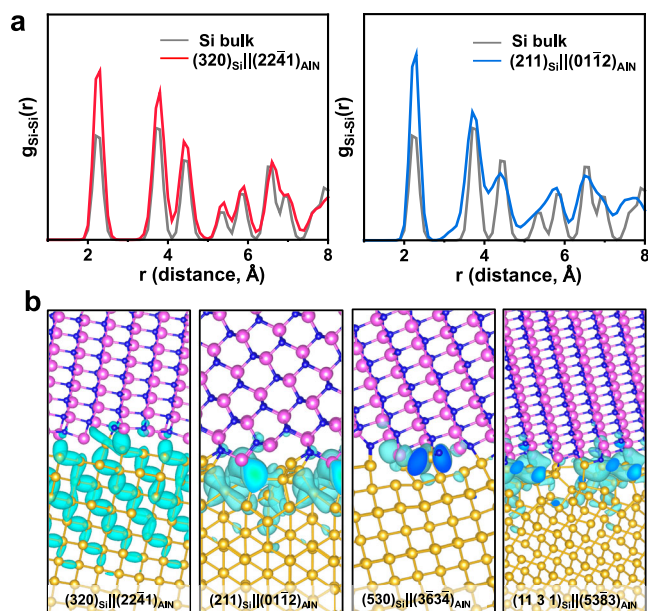


**Fig. 4 | Radial distribution function and electronic structures of selected low-polar Si/AlN interfaces.** **a** Radial distribution function  $g(r)$  of Si-Si for bulk Si and two low-polar interfaces. **b** Partial charge densities of valence band maximum (VBM) for four low-polar interfaces.

lattice positions, effectively passivating dangling bonds. This ordered arrangement of atoms is evident from the Radial Distribution Function (RDF), which displays sharp peaks closely matching those of bulk Si and AlN (see Fig. 4a). In contrast, the boundary atoms in other low-polar interfaces are disordered, characterized by numerous dangling bonds and broader RDF peaks (see Figs. 2 and 4a). The electronic structure at  $(320)_{\text{Si}} || (22\bar{4}1)_{\text{AlN}}$  interface also confirms the well-ordered interface structure. For example, Fig. 4b shows that the valence band maximum (VBM) of  $(320)_{\text{Si}} || (22\bar{4}1)_{\text{AlN}}$  is delocalized, whereas the VBM of other low-polar interfaces are localized.

It might be emphasized that such a perfect match between high-index Si and high-index AlN surfaces is rare, considering that high-index surfaces typically involve complex surface geometries such as steps and kinks. In fact, as shown from our interface search, other low-polar Si/AlN interfaces do show atomic mismatches between Si and AlN with rich interface reconstructions and defects.

As an important indicator to the lifespan of LEDs, the interfacial thermal conductance (ITC) was calculated using non-equilibrium molecular dynamics (NEMD, see Supplemental Note 6 for calculation details) based on the G-MBNN potential. It is noteworthy that the thermal conductance between Si and AlN is phonon-mediated due to the absence of free electrons within this system. Interestingly, the ITCs across 7 low-polar interfaces range from 0.41 to 0.50  $\text{GWm}^{-2}\text{K}^{-1}$ , surpassing those of 4 polar interfaces ranging from 0.32 to 0.39  $\text{GWm}^{-2}\text{K}^{-1}$  (see red bars in Fig. 3a). This indicates that high-index Si orientations do not adversely affect the ITC property; specifically, the ITC of  $(320)_{\text{Si}} || (22\bar{4}1)_{\text{AlN}}$  is 0.47  $\text{GWm}^{-2}\text{K}^{-1}$ , positioning it among those interfaces exhibiting some of the highest ITC values available today when comparing it against existing benchmarks; notably, TiN/MgO has demonstrated superior phonon-mediated ITC performance thus far with a measurement reaching up to 0.7  $\text{GWm}^{-2}\text{K}^{-1}$ —an achievement attributing to both TiN and MgO sharing similar rocksalt structures. Other interfaces typically exhibit thermal conductance ranging from 0.08  $\text{GWm}^{-2}\text{K}^{-1}$  to 0.3  $\text{GWm}^{-2}\text{K}^{-1}$  (e.g. Si/Al: 0.35  $\text{GWm}^{-2}\text{K}^{-1}$ , Al/AlN: 0.23  $\text{GWm}^{-2}\text{K}^{-1}$ , Al/Al<sub>2</sub>O<sub>3</sub>: 0.18  $\text{GWm}^{-2}\text{K}^{-1}$ )<sup>15,35–37</sup>. Clearly, the identified ITC value for our  $(320)_{\text{Si}} || (22\bar{4}1)_{\text{AlN}}$  (0.47  $\text{GWm}^{-2}\text{K}^{-1}$ ) stands out, being only lower than the best TiN/MgO. This suggests the great potential of  $(320)_{\text{Si}} || (22\bar{4}1)_{\text{AlN}}$  for applications that require high heat dissipation.

The variation of ITC in different Si/AlN interfaces can be understood by analyzing the phonon correlation factor (S) that is defined as

$$S = \frac{(\int_0^\infty \sqrt{P_1(\omega)P_2(\omega)}d\omega)^2}{\int_0^\infty P_1(\omega)d\omega \int_0^\infty P_2(\omega)d\omega} \quad (3)$$

where  $\omega$  is phonon frequency,  $P_1(\omega)$  and  $P_2(\omega)$  are the partial phonon density of states (PPDOS) of two materials. The value of S quantifies the overlap of PPDOS between the two phases, ranging from 0 to 1. A higher value of the phonon correlation factor S corresponds to a better phonon coupling, and thus allows an easier heat pass through the interface.

Figure 3b shows the cross-interface-plane PPDOS for two Si/AlN interfaces (the data for other interfaces are provided in Supplemental Fig. 8–18) using NEMD trajectory from 0.7 nm Si and 0.7 nm AlN layers near the interface. It is evident that the phonon frequencies of AlN are higher than those of Si. The computed phonon correlation factor S of Si/AlN interfaces ranges from 0.39 to 0.56, where the  $(320)_{\text{Si}} || (22\bar{4}1)_{\text{AlN}}$  interface exhibits the highest S value (0.56), which is apparently related to its highly ordered atomic structure. Figure 3c depicts the correlation between S and ITC, revealing a good linear relation fitted as  $G = 0.88 \times S - 0.022$  with an  $R^2$  value of 0.91. To prove the ITC is an interface property, we also calculated S using NEMD trajectories from thicker Si and AlN layers of the Si/AlN interface. When the thickness exceeds 1.5 nm, the S values of different Si/AlN interfaces converge to a similar value of 0.40, showing a poor correlation between S and ITC with an  $R^2$  value of 0.42 (see Supplemental Fig. 19). This indicates that the ITC is governed by the phonon coupling of near-interface atomic motions, i.e. within approximately 0.70 nm thickness of the Si/AlN interface.

To summarize, we employed an enhanced ML-interface method to explore all potential Si/AlN interfaces. The high-index Si(320) emerges as the optimal substrate for AlN growth, characterized by a low interface energy of 1.57 J/m<sup>2</sup>, minimal polarization at 0.20 C/m<sup>2</sup>, and high interface thermal conductivity of 0.47  $\text{GWm}^{-2}\text{K}^{-1}$ . While our findings indicate that  $(320)_{\text{Si}} || (22\bar{4}1)_{\text{AlN}}$  is a suitable interface for LED applications, we demonstrate that the power of ML-based approach in screening solid-solid interfaces, which offers an efficient and general pathway for designing new semiconductor materials through epitaxial growth.

## Methods

In this study, we enhance the ML-interface method in two significant ways. First, we introduce a new OR screening algorithm that substantially accelerates the computational efficiency. Second, we establish a many-body function corrected neural network potential (G-MBNN)<sup>38</sup> specifically for the Si-Al-N ternary system, which enables rapid interface structure searches while accurately accounting for variations in all possible chemical compositions (Al: N: Si). They are elaborated as follows.

The new OR screening algorithm utilizes Eq. 4 that replaces the original Eq. 5 in finding the lattice correspondence matrices  $\mathbf{F}$  from its transpose  $\mathbf{F}^T$ .

$$\mathbf{F}^T = \mathbf{M}^T \mathbf{H}_B \mathbf{U} \mathbf{H}_A^{-1} (\mathbf{T}^T)^{-1} \quad (4)$$

$$\mathbf{F}^T = \mathbf{M}^T \mathbf{B}^T (\mathbf{A}^T)^{-1} (\mathbf{T}^T)^{-1} \quad (5)$$

In Eq. 5,  $\mathbf{T}$  and  $\mathbf{M}$  are the primitive lattice parameters of two phases (they are Si and AlN lattices in this work);  $\mathbf{A}$  and  $\mathbf{B}$  denote transformation matrices to match two lattices, which can be randomly specified to obtain  $\mathbf{F}$ . Apparently, given a pair of  $\mathbf{A}$  and  $\mathbf{B}$ , all pairs of  $\mathbf{U}\mathbf{A}$  and  $\mathbf{U}\mathbf{B}$  also generate the same  $\mathbf{F}$ , where  $\mathbf{U}$  is an any unimodular matrix. To remove the redundant  $\mathbf{F}$  in Eq. 5, we employ the Hermite normal form

to decompose the integer matrices **A** and **B**, which leads to Eq. 4. Here, **H<sub>A</sub>** and **H<sub>B</sub>** are two integral lower triangular matrices, with entries  $h_{ij}$  satisfying the conditions: (i)  $h_{ij} = 0$  for  $j > i$ ; (ii)  $h_{ii} > 0$ ; (iii)  $0 \leq h_{ij} < h_{ii}$  for  $j < i$ . It can be proved that **F** derived from all likely pairs of **A** and **B** is a unique set of **{H<sub>A</sub>, U, H<sub>B</sub>}**<sup>39,40</sup>. Thus, one can generate the lattice correspondence **F** by exploring the sets of **{H<sub>A</sub>, U, H<sub>B</sub>}**, as shown in Eq. 4. More details can be found in ref. 40 and the Supplemental Note I.

The latest G-MBNN<sup>38</sup> potential of the ternary Si-Al-N system in combination with the stochastic surface walking (SSW) global optimization<sup>41,42</sup> is utilized for the interface search. The G-MBNN potential can better account for the complex interface structure, both in the chemical composition variation and the long-range interaction of defects/dislocations. All reported low energy structures from G-MBNN potential calculations have been further refined by density functional theory (DFT) (see Supplemental Note 4 and Supplemental Note 7 for details). All atomic simulations are performed using Large-scale Atomic Simulation with Neural Network Potential (LASP)<sup>43</sup> program developed in our group<sup>31,38</sup>. The benchmark of Si-Al-N G-MBNN potential against density functional theory (DFT) calculations and all simulation details, including energies, structures, and interfacial thermal conductances, are provided in Supplementary Information.

### Reporting summary

Further information on research design is available in the Nature Portfolio Reporting Summary linked to this article.

### Data availability

The data generated in this study are provided in the Source Data file and can also be obtained from the corresponding authors upon request. Source data are provided with this paper.

### Code availability

The software code of LASP and NN potential generated in this study has been deposited on the website [<http://www.lasphub.com>](<http://www.lasphub.com>). The LASP binary code for the Si-Al-N system is available under accession code (<http://www.lasphub.com/supportings/lasp-SiAlN.tgz>), and the Si-Al-N G-MBNN potential is available at (<http://www.lasphub.com/supportings/SiAlN.pot>). The code is available upon request from the corresponding authors or via the provided website.

### References

1. Tanaka, A., Choi, W., Chen, R. & Dayeh, S. A. Si complies with GaN to overcome thermal mismatches for the heteroepitaxy of thick gan on Si. *Adv. Mater.* **29**, 1702557 (2017).
2. Boles T. GaN-on-silicon present challenges and future opportunities. In: *2017 12th European Microwave Integrated Circuits Conference (EuMIC)* (2017).
3. Dadgar, A. Sixteen years GaN on Si. *Phys. Status. Solidi. (b)* **252**, 1063–1068 (2015).
4. Semond, F. Epitaxial challenges of GaN on silicon. *MRS Bull.* **40**, 412–417 (2015).
5. <https://www.gminsights.com/industry-analysis/gan-led-chips-market>.
6. King, S. W., Nemanich, R. J. & Davis, R. F. Band alignment at AlN/Si (111) and (001) interfaces. *J. Appl. Phys.* **118**, 045304 (2015).
7. Dasgupta, S., Wu, F., Speck, J. S. & Mishra, U. K. Growth of high quality N-polar AlN(0001) on Si(111) by plasma assisted molecular beam epitaxy. *Appl. Phys. Lett.* **94**, 151906 (2009).
8. Raghavan, S. & Redwing, J. M. In situ stress measurements during the MOCVD growth of AlN buffer layers on (111) Si substrates. *J. Cryst. Growth* **261**, 294–300 (2004).
9. Abdallah, B. et al. Thickness and substrate effects on AlN thin film growth at room temperature. *Eur. Phys. J. Appl. Phys.* **43**, 309–313 (2008).
10. Lebedev, V., Schröter, B., Kipshidze, G. & Richter, W. The polarity of AlN films grown on Si(111). *J. Cryst. Growth* **207**, 266–272 (1999).
11. Murase, T., Tanikawa, T., Honda, Y., Yamaguchi, M. & Amano, H. Optical properties of (1-101) InGaN/GaN MQW stripe laser structure on Si substrate. *Phys. Status. Solidi. (c)* **8**, 2160–2162 (2011).
12. Ni, X. et al. Nonpolar m-plane GaN on patterned Si(112) substrates by metalorganic chemical vapor deposition. *Appl. Phys. Lett.* **95**, 111102 (2009).
13. Tomita, K., Hikosaka, T., Kachi, T. & Sawaki, N. Mg segregation in a (1-101) GaN grown on a 7° off-axis (001) Si substrate by MOVPE. *J. Cryst. Growth* **311**, 2883–2886 (2009).
14. Sawaki, N. et al. Growth and properties of semi-polar GaN on a patterned silicon substrate. *J. Cryst. Growth* **311**, 2867–2874 (2009).
15. Minnich, A. J. et al. Thermal conductivity spectroscopy technique to measure phonon mean free paths. *Phys. Rev. Lett.* **107**, 095901 (2011).
16. Li, Y.-H. et al. Atomic-scale probing of heterointerface phonon bridges in nitride semiconductor. *Proc. Natl. Acad. Sci.* **119**, e2117027119 (2022).
17. Giri, A. & Hopkins, P. E. A review of experimental and computational advances in thermal boundary conductance and nanoscale thermal transport across solid interfaces. *Adv. Funct. Mater.* **30**, 1903857 (2020).
18. Boo, J. H. et al. Growth of AlN and GaN thin films on Si(100) using new single molecular precursors by MOCVD method. *Phys. Status. Solidi. (a)* **176**, 711–717 (1999).
19. Chen, P. et al. Growth of high quality GaN layers with AlN buffer on Si(111) substrates. *J. Cryst. Growth* **225**, 150–154 (2001).
20. Lumbantoruan, F. et al. Investigation of TMAI preflow to the properties of AlN and GaN film grown on Si(111) by MOCVD. In: *2014 IEEE International Conference on Semiconductor Electronics (ICSE2014)* (2014).
21. Zhu, D., Wallis, D. J. & Humphreys, C. J. Prospects of III-nitride optoelectronics grown on Si. *Rep. Prog. Phys.* **76**, 106501 (2013).
22. Wang, X., Li, H., Wang, J. & Xiao, L. The effect of Al interlayers on the growth of AlN on Si substrates by metal organic chemical vapor deposition. *Electron. Mater. Lett.* **10**, 1069–1073 (2014).
23. Liu, R., Ponce, F. A., Dadgar, A. & Krost, A. Atomic arrangement at the AlN/Si (111) interface. *Appl. Phys. Lett.* **83**, 860–862 (2003).
24. Contreras, O. E., Ruiz-Zepeda, F., Dadgar, A., Krost, A. & Ponce, F. A. Atomic Arrangement at the AlN/Si(110) Interface. *Appl. Phys. Express* **1**, 061104 (2008).
25. Ding, K. et al. Recent progress in nonpolar and semi-polar GaN light emitters on patterned Si substrates. *Proceedings, Gallium Nitride Materials and Devices XIII* **10532**, 6–21 (2018).
26. Ravash, R. et al. Metal organic vapor phase epitaxy growth of single crystalline GaN on planar Si(211) substrates. *Appl. Phys. Lett.* **95**, 242101 (2009).
27. Yang, M. et al. Maskless selective growth of semi-polar (112̄2) GaN on Si (311) substrate by metal organic vapor phase epitaxy. *J. Cryst. Growth* **311**, 2914–2918 (2009).
28. Tanikawa, T., Kagohashi, Y., Honda, Y., Yamaguchi, M. & Sawaki, N. Reduction of dislocations in a (112-2)GaN grown by selective MOVPE on (113)Si. *J. Cryst. Growth* **311**, 2879–2882 (2009).
29. Zhang, B. & Xiang, P. Preparation method for semi-polar non-polar GaN self-support substrate Patent CN102214557A.
30. Li, Y.-F. & Liu, Z.-P. Smallest stable Si/SiO<sub>2</sub> interface that suppresses quantum tunneling from machine-learning-based global search. *Phys. Rev. Lett.* **128**, 226102 (2022).
31. Ji-Li, L. & Ye-Fei, L. Recent advances in the interface structure prediction for heteromaterial systems. *J. Mater. Inf.* **3**, 22 (2023).
32. Asbóth, J. K., Oroszlány, L. & Pályi, A. Polarization and Berry Phase. In: *A Short Course on Topological Insulators: Band Structure and Edge States in One and Two Dimensions* (eds Asbóth J. K., Oroszlány L., Pályi A.). Springer International Publishing (2016).
33. Kim, Y. H., Lee, J. H., Noh, Y. K., Oh, J. E. & Ahn, S. J. Microstructural characteristics of AlN thin layers grown on Si(110) substrates by

- molecular beam epitaxy: Transmission electron microscopy study. *Thin Solid Films* **576**, 61–67 (2015).
34. Olshanetsky, B. Z. & Mashanov, V. I. LEED studies of clean high Miller index surfaces of silicon. *Surf. Sci.* **111**, 414–428 (1981).
  35. Costescu, R. M., Wall, M. A. & Cahill, D. G. Thermal conductance of epitaxial interfaces. *Phys. Rev. B* **67**, 054302 (2003).
  36. Lyeo, H.-K. & Cahill, D. G. Thermal conductance of interfaces between highly dissimilar materials. *Phys. Rev. B* **73**, 144301 (2006).
  37. Olson, J. R. et al. Thermal conductivity of diamond between 170 and 1200 K and the isotope effect. *Phys. Rev. B* **47**, 14850–14856 (1993).
  38. Kang, P.-L., Yang, Z.-X., Shang, C. & Liu, Z.-P. Global Neural Network Potential with Explicit Many-Body Functions for Improved Descriptions of Complex Potential Energy Surface. *J. Chem. Theory Comput.* **19**, 7972–7981 (2023).
  39. Cohen H. *A course in computational algebraic number theory*. Springer Science & Business Media (2013).
  40. Wang, F.-C., Ye, Q.-J., Zhu, Y.-C. & Li, X.-Z. Crystal-Structure Matches in Solid-Solid Phase Transitions. *Phys. Rev. Lett.* **132**, 086101 (2024).
  41. Shang, C. & Liu, Z.-P. Stochastic surface walking method for structure prediction and pathway searching. *J. Chem. Theory Comput.* **9**, 1838–1845 (2013).
  42. Hu, Z.-Y., Luo, L.-H., Shang, C. & Liu, Z.-P. Free Energy Pathway Exploration of Catalytic Formic Acid Decomposition on Pt-Group Metals in Aqueous Surroundings. *ACS Catal.* **14**, 7684–7695 (2024).
  43. Huang, S.-D., Shang, C., Kang, P.-L., Zhang, X.-J. & Liu Z.-P. LASP: Fast global potential energy surface exploration. *Wiley Interdisciplinary Reviews-Computational Molecular Science* **9**, (2019).

## Acknowledgements

This work received financial support from the National Science Foundation of China (12188101, 22033003, 22122301, 92472113), the National Key Research and Development Program of China (2022YFA1503503, 2024YFA1509600), the Fundamental Research Funds for the Central Universities (20720220011), Science & Technology Commission of Shanghai Municipality (2024ZDSYS02), the Natural Science Foundation of Shanghai (24ZR1405100), and the Tencent Foundation for XPLOER PRIZE.

## Author contributions

Z. L. and Y. L. conceived the project and contributed to the design of the calculations and analyses of the data. J. L. carried out most of the

calculations and wrote the first version of the paper. All the authors discussed the results and commented on the manuscripts.

## Competing interests

The authors declare no competing interests.

## Additional information

**Supplementary information** The online version contains supplementary material available at <https://doi.org/10.1038/s41467-025-59613-5>.

**Correspondence** and requests for materials should be addressed to Ye-Fei Li or Zhi-Pan Liu.

**Peer review information** *Nature Communications* thanks Xin-Zheng Li, who co-reviewed with Fangcheng Wang, and the other, anonymous, reviewer(s) for their contribution to the peer review of this work. A peer review file is available.

**Reprints and permissions information** is available at <http://www.nature.com/reprints>

**Publisher's note** Springer Nature remains neutral with regard to jurisdictional claims in published maps and institutional affiliations.

**Open Access** This article is licensed under a Creative Commons Attribution-NonCommercial-NoDerivatives 4.0 International License, which permits any non-commercial use, sharing, distribution and reproduction in any medium or format, as long as you give appropriate credit to the original author(s) and the source, provide a link to the Creative Commons licence, and indicate if you modified the licensed material. You do not have permission under this licence to share adapted material derived from this article or parts of it. The images or other third party material in this article are included in the article's Creative Commons licence, unless indicated otherwise in a credit line to the material. If material is not included in the article's Creative Commons licence and your intended use is not permitted by statutory regulation or exceeds the permitted use, you will need to obtain permission directly from the copyright holder. To view a copy of this licence, visit <http://creativecommons.org/licenses/by-nc-nd/4.0/>.

© The Author(s) 2025